



Effect of printing parameters on extrusion-based additive manufacturing using highly filled CuSn12 filament

Beatrice Aruanno¹ · Alessandro Paoli¹ · Armando Viviano Razionale¹ · Francesco Tamburrino¹

Received: 19 January 2023 / Accepted: 6 July 2023
© The Author(s) 2023

Abstract

Typical additive manufacturing (AM) processes for producing metal and ceramic parts are highly energy-consuming and expensive to install and maintain. On the other hand, material extrusion AM (MEAM) technologies are conventionally used to produce polymeric parts but only marginally to process metallic materials. A feasible alternative is to process polymeric filaments loaded with metal particles. Debinding and sintering processes are then required to join the metal particles and obtain the final parts. In recent years, highly filled metal filaments consisting of a polymer loaded with a high concentration of metal powder have been commercialized for this purpose. In this study, the printability of a commercial CuSn12 filament was investigated by evaluating the influence of the process parameters on the density, shrinkage, porosity, and mechanical properties of the additively manufactured samples using a low-cost desktop 3D printer. Parameters such as the flow rate and ironing had the greatest influence on the density of the green samples. The correct selection of these parameters may reduce shrinkage after sintering. Furthermore, the obtained bronze had a notable ultimate tensile strength (mean value of 107 MPa), high stiffness (E values range from 38 to 50 GPa), and a greater elongation at break (mean value of 13%) than that of cast bronze of the same CuSn12 type. In this case, the extrusion pattern and ironing had the most significant influence on the final mechanical performance. The study provides insights into the use of highly filled bronze filaments combined with MEAM to produce functional parts for engineering applications.

Keywords Metal material extrusion · Printing parameters · Highly filled bronze filament · Mechanical properties · Shrinkage

1 Introduction

Additive manufacturing (AM) is an increasingly widespread production technology that directly creates a product from a computer-aided design (CAD) model through layer-by-layer material addition. Currently, the most commonly used AM materials include polymers, metals, ceramics, and composites. The application range of AM products is highly connected to the materials adopted, and even if polymers are the most widely used AM materials, industrial and academic efforts are increasingly oriented towards the investigation of metal AM technologies due to the superior mechanical properties of the manufactured products [1, 2]. The most common AM processes for metals are powder bed fusion

(PBF) and direct energy deposition (DED) [3–5]. However, these technologies are generally high-energy consuming, expensive to install and maintain, and require a cooling system and an inert gas environment to prevent oxidation. In addition, they cause a significant amount of powder waste during manufacturing, which is a handling hazard.

On the other hand, material extrusion additive manufacturing (MEAM) technologies, which are conventionally used to produce polymeric parts [6, 7], are less commonly used to process metallic materials. However, among these AM techniques, MEAM promises to be the most cost-effective option because of its smaller initial and overall investment costs, faster building rates, and greater production flexibility [8]. Moreover, MEAM minimizes material waste because all of the powder contained within the filament is used during the printing process. Three different approaches characterize MEAM: filament-based, plunger-based, and screw-based approaches [9, 10]. Among these, filament-based techniques, also known as fused filament fabrication (FFF), are the most

✉ Francesco Tamburrino
francesco.tamburrino@unipi.it

¹ Department of Civil and Industrial Engineering, University of Pisa, Largo Lucio Lazzarino, 56122 Pisa, Italy

widely adopted. In FFF, a filament is heated and melted in an extruder and deposited in layers through a nozzle. To date, FFF has not been used to directly fabricate metallic parts characterized by high melting temperatures. The idea of using filaments consisting of a polymer loaded with metal particles dates back to the late 1990s [11, 12]. This 3D printing process is carried out by extruding the filament at a temperature higher than the melting point of the binder polymer. The 3D-printed part is the so-called green part from which the polymer binder is removed by a debinding process. The remaining metal powders are then fused together through a conventional sintering step to define the brown part, which has superior mechanical properties. The maximum metal content of the filament is limited by its rheological behavior because the filament must maintain extrudability as well as a suitable stiffness-to-flexibility ratio [13–15]. On the other hand, higher metal contents reduce the porosity of the part and consequently the shrinkage after the sintering process [8]. However, studies have only recently focused extensively on the use of highly filled (HF) metal filaments to fabricate parts with significant mechanical properties. HF metal filaments contain a high volume percentage of metal particles, typically between 50 and 65 vol% [16]. Two strategies can be followed: self-making the filament by mixing metal particles and binders, or using commercial filaments to streamline the process and encourage the use of low-level desktop printers. MEAM-HF has shown great potential as a feasible cost-effective alternative for the fabrication of metallic parts using different metals, such as bronze [17–21], copper [20, 22–26], iron [20, 27, 28], steel [11, 28–45], and titanium [46–48].

In recent years, innovative formulations of filaments consisting of a polymer loaded with a high concentration of metal powder have been made commercially available. Among commercial HF metal filaments, the Ultrafuse® (BASF 3D Printing Solutions GmbH) [49] and the “Filamet™” (the virtual foundry) [50] are the most commonly adopted. In particular, The Virtual Foundry has developed a range of sinterable metal filaments, which is probably the widest available on the market. There is a growing need to investigate the characteristics of MEAM metal parts for real-world applications in terms of dimensional accuracy and mechanical properties because commercial metal filaments and processes are relatively new. The shrinkage of sintered parts produced by MEAM is indeed a critical issue, which stems from the significant porosity of the green parts, resulting from the debinding process. Shrinkage is a more significant issue in MEAM than laser melting processes using metal powders since MEAM requires binding agents that constitute a finite volume of the deposited material that is removed upon sintering. During the debinding stage, the removal of binder materials may leave voids within the green parts, and when these parts undergo

sintering, the residual porosity leads to shrinkage, causing dimensional variations between the design model and the final part. This represents one of the most significant challenges in enhancing the acceptance of 3D-printed parts for potential functional applications. This challenge surely requires a careful optimization of both debinding and sintering, but also printing parameters play a crucial role [31, 51].

In the present study, a preliminary investigation on the printability of bronze filaments (Bronze Filamet™) manufactured by The Virtual Foundry is carried out. The work provides novel experimental insights regarding the printability of the CuSn12 filament and the effects of the printing parameters on the mechanical properties of the additively manufactured parts. To the best of the author’s knowledge, there is scarce scientific evidence about the characterization of the mechanical properties of highly-filled CuSn12 filaments produced by MEAM and sintered in an air environment. Bronze parts have many important engineering applications and are often used in liquid environments owing to their corrosion resistance, particularly for marine and railway components, such as ship propellers, valves, and pumps [52, 53]. Furthermore, the production of bronze parts with complex shapes allows the design of bespoke and patient-specific appliances for biomedical applications. For example, 3D-printed bronze shields can effectively reduce radiation doses to adjacent healthy tissues in surface radiation treatments [17].

The aim of the present study is to investigate the influence of the most significant printing parameters on the porosity of additively manufactured metal parts using a low-cost desktop FFF machine. According to the available literature, very few studies have investigated the influence of process parameters on the mechanical properties of samples obtained using bronze Filamet™ [18, 19, 21]. Zhang et al. proposed a machine learning approach to predict dimensional variations in MEAM bronze parts after 3D printing and sintering processes, with the aim of optimizing the printing and sintering process parameters [18]. Their study focused on the following parameters: layer thickness, nozzle temperature, and printing speed. Wei et al. studied the influence of printing and sintering directions on shrinkage, tensile properties, and porosity of sintered parts [21]. In-depth microstructure and phase analysis of 3D-printed bronze filaments have previously been carried out, and some mechanical properties (i.e., flexural strength and elastic modulus) have been evaluated [19]. However, these studies focused on investigating and analyzing some specific characteristics of manufactured parts. In the present study, a systematic and multiscale approach was developed by considering the influence of different printing parameters (i.e., nozzle temperature, flow rate, infill pattern, and ironing) on the porosity,

density, shrinkage, and mechanical properties (i.e., elastic modulus, ultimate tensile strength, and stress-strain curves) of the final metal samples.

2 Materials and methods

2.1 Materials

A bronze-PLA filament (Bronze Filamet™) supplied by The Virtual Foundry (Stoughton, WI, USA) [50] was used to print the green parts. The filaments were analyzed by scanning electron microscopy (SEM) using an FEI Quanta 450 ESEM-FEG (FEI Europe BV, Eindhoven, The Netherlands).

The internal structure of the filament was composed of spherical metal particles with dimensions varying from 10 to 50 μm dispersed within the polymeric binder (Fig. 1). The filament contained 87 to 90% metal powder by weight and had a density of 4.29 to 4.5 g/cm³. The bronze powder, as confirmed by the energy-dispersive spectroscopy (EDS), is composed of 88–91% and 9–12% of copper and tin, respectively, by weight.

Two specimen types were identified to study the tensile properties and shrinkage of the 3D-printed material after

thermal postprocessing. The geometries of both specimen types were modelled using SolidWorks® and sliced using Ultimaker Cura® 4.9.1.

The geometry of the tensile specimen (Fig. 2) was designed to allow placement in the crucible for thermal post-processing. A simple prismatic specimen (nominal dimensions 21 × 8.4 × 4.2 mm³ in the x, y, and z directions, respectively, where z is the direction normal to the building platform) was instead used to ensure volume, density, and shrinkage measurements with a high degree of accuracy.

2.2 3D printing

3D printing was carried out using the low-cost desktop FFF machine MINGDA D2, which is characterized by a printing volume of 230 × 230 × 260 mm³, maximum nozzle temperature of 260 °C, and maximum bed temperature of 100 °C.

The 3D printing machine equipped with a *direct drive extruder* mounted on the printhead was modified by replacing the common brass nozzle with a 0.6 mm stainless steel nozzle. This modification was required to minimize nozzle wear caused by metal particles in the filament. The direct drive extruder was used in this study because of the mechanical properties of the selected filament, which has a diameter of 1.75 mm, and is characterized by a significant

Fig. 1 Analysis of the cross-section of the Bronze Filamet™ filament by scanning electron microscopy (SEM) and analysis of its chemical composition (EDS)

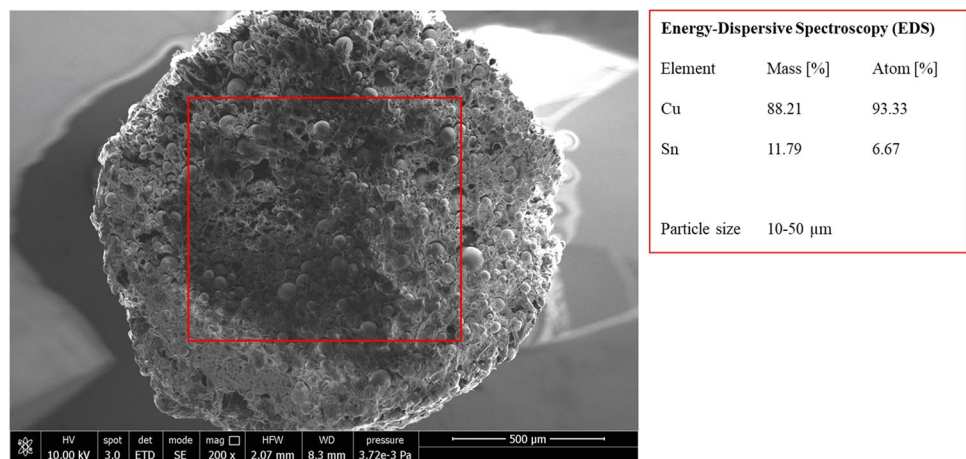
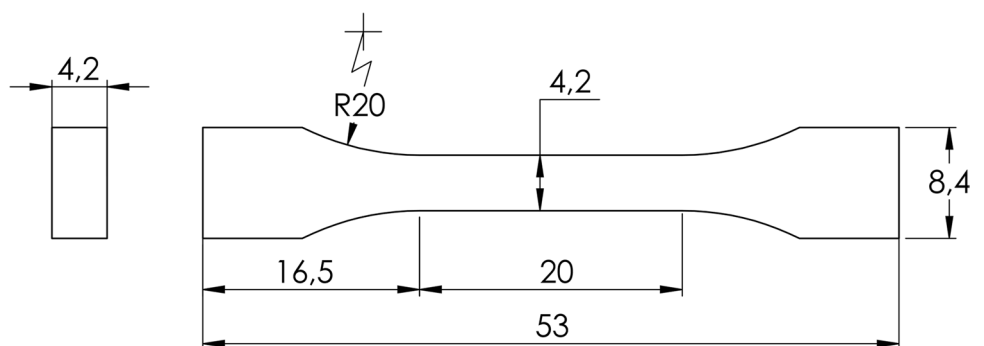


Fig. 2 Dog-bone tensile specimen's geometry with associated dimensions



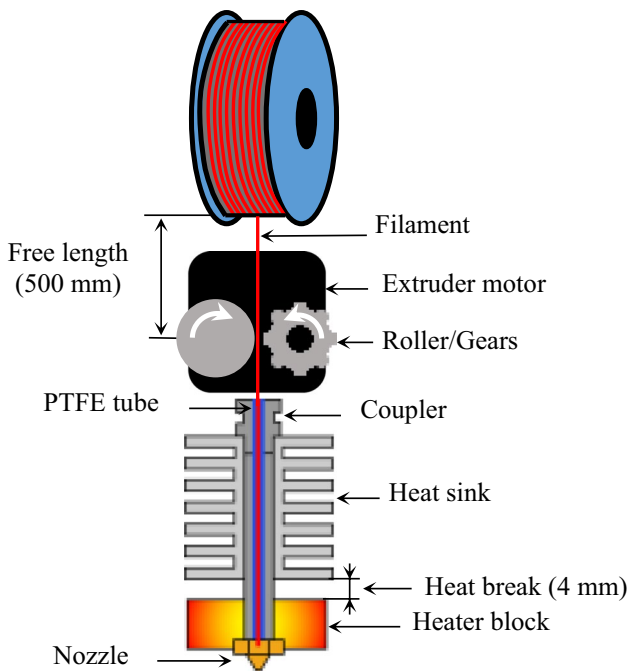


Fig. 3 Schematic view of the cross-section of the adopted FFF direct drive extruder

Table 1 Main printing parameters suggested by the filament manufacturer (The Virtual Foundry)

Parameters	Value
Printing temperature (°C)	205–215
Building platform temperature (°C)	50
Flow rate (mm ³ /s)	2.16
Nozzle diameter (mm)	≥ 0.6 (stainless steel)

brittleness due to the high metal particle content (> 85%). A *Bowden extruder* would greatly impair the printing process because the filament feeder is not directly mounted on the printhead. However, because the filament feeder is placed on the printer frame, the filament travels through a polytetrafluoroethylene (PTFE) tube to reach the hot end.

A schematic representation of the adopted 3D printing equipment is reported in Fig. 3.

2.2.1 3D printing settings

The Virtual Foundry has suggested some printing parameters for this material, which are summarized in Table 1. Nine sets consisting of 5 dog-bone specimens have been 3D-printed using different combinations of parameters. Each experimental set was assigned a letter (from A to I). The parameters investigated were selected for their recognized influence on the density and on the reduction of unwanted voids for parts printed by FFF technology [54, 55]. Starting from the suggested options, the first parameter examined was the flow rate. The starting point for the definition of the parameter sets was provided by the filament supplier, which suggested specific settings for the nozzle temperature, printing bed temperature, and flow rate. Set A was exactly defined in accordance with the supplier’s guidelines and thus represents the base set, which is useful for comparison. However, the flow rate of 2.16 mm³/s resulted in specimens with excessive voids. For this reason, after preliminary tests, it was decided to increase the flow rate till 2.92 mm³/s (135% of the initial value). This value allowed us to get a better infill of the specimen, with no visible macroscopic inter-raster and inter-layer voids. All the sets (B–I) share this flow rate value. The studied parameters were nozzle temperature, the pattern of intermediate layers, and ironing and varied on two levels. Table 2 summarizes the sets with the different combinations of printing parameters.

The flow rate is the volume of filament per second (mm³/s) that passes through the nozzle. The nozzle temperature is the temperature of the nozzle during material extrusion. Generally, a higher nozzle temperature reduces the polymer viscosity; thus, the presence of unwanted voids improves polymer melt flowability and interlayer bonding. However, excessively elevated temperatures can cause dimensional and geometric deviations in the printed parts. In the present study, layers 1 to 4 and 11 to 14 were the top and bottom layers, respectively, while the remaining layers were defined as intermediate layers. A 100% infill density was adopted for the bottom, top, and intermediate layers. An extrusion *concentric* pattern was selected for the bottom and top layers, whereas *lines* or *concentric* patterns were selected

Table 2 The experimental printing parameter sets, ranging from set A to set I. Set A represents the reference from the filament supplier. The two concentric circles and the two parallel lines are respectively representative of *concentric* and *lines* pattern of extrusion

Set	A	B	C	D	E	F	G	H	I
Flow rate (mm ³ /s)	2.16	2.92	2.92	2.92	2.92	2.92	2.92	2.92	2.92
Nozzle temperature (°C)	210	210	210	210	220	220	210	220	220
Pattern of intermediate layers (5-10)	⊙	⊙	//	⊙	//	⊙	//	⊙	//
Ironing	-	-	-	yes	-	-	yes	yes	yes

for the intermediate layers. The ironing process can be considered a post-processing technique aimed at improving the surface finishing of parts produced by the FFF. The ironing process consists of an additional pass over the top surface of the printed layer with the extruder nozzle (Fig. 4a). When the nozzle passes over the top surface again, the material melts (in our case, the PLA binder), creating a smoother surface (Fig. 4b). Furthermore, the pressure of the filament in the nozzle is kept high by the feeder so that the creases on the surface are filled with material, and the treated layer is flattened by removing peaks caused by tool paths during the layer deposition.

Ironing reduces unwanted voids caused by the printing process, average surface roughness, and warping of FFF-ABS parts [56]. Generally, this process is applied to the last layer to improve the finishing of the upper surface of the part, thus increasing aesthetic results. In this study, however, ironing was used on multiple layers (after layers 3, 6, 8, 11, and 14) to increase the density of the printed parts (and eventually contrast the excessive shrinking during sintering). Clearly, the drawbacks of this approach are a significant increase in printing time and possible over-extrusion with a loss of dimensional accuracy.

Table 3 reports the parameters common to all experimental sets. In particular, filament retraction, which is usually adopted to retract the filament at the end of an active movement to keep the printed surface clean, has been disabled owing to the brittle behavior of the metal filament. For the same reason, the printing speed was lowered with respect to the maximum value suggested by The Virtual Foundry. Finally, the building platform temperature and the printing cooling options were set according to the recommendations of the filament manufacturer.

2.3 Debinding and sintering

The sintering process was carried out using a Metal 3D printing Starter kiln made by Sapphire 3D (Chicago, IL, USA) [57]. The kiln has a sintering chamber with dimensions of $152 \times 152 \times 159 \text{ mm}^3$ and a maximum

Table 3 Printing parameters common to all the experimental sets

Parameters	Value
Wall thickness (mm)	1.8
Layer thickness (mm)	0.3
Line width (mm)	0.6
Building platform temperature (°C)	50
Printing speed (mm/s)	12
Retraction	None
Printing cooling	None
Bottom/top layers (1–4; 11–14) pattern	⊙

temperature of $1370 \text{ }^\circ\text{C}$. A three-button controller allows for the handling of thermal cycles in terms of temperature ramps and holding times. Two different post-processing thermal treatments (debinding and sintering) are sequentially carried out inside the kiln. The purpose of the first heating phase is to debind the PLA, which is turned into a gas and vented out from the kiln. Next, a second cycle is adopted with a greater maximum temperature to sinter the metal particles, thus creating the brown part.

The green parts are placed in the kiln using a crucible. Aluminum oxide powder is used to completely cover the green parts during the thermal process, thus providing uniform heating and supporting the part when it softens during sintering. The kiln is not equipped with a vacuum or a controlled atmosphere chamber. For this reason, powdered carbon is placed on top of the aluminum oxide powder to burn off oxygen in the chamber during sintering and prevent oxidation of the metal parts. As opposed to the aluminum oxide powder that can be reused, the powdered carbon layer must be replaced in each cycle.

Figure 5 lists the temperature profiles suggested by the filament supplier adopted to carry out the debinding and sintering processes. It is worth noting that the sintering temperature exceeds the maximum sintering temperature suggested in the study by Lu et al. [19] ($832 \text{ }^\circ\text{C}$) to prevent the formation of oxidation reactions. However, the

Fig. 4 Schematic of the ironing procedure and the path followed by the nozzle during this process (a). Zoom of an example specimen 3D-printed without and with the ironing process (b)

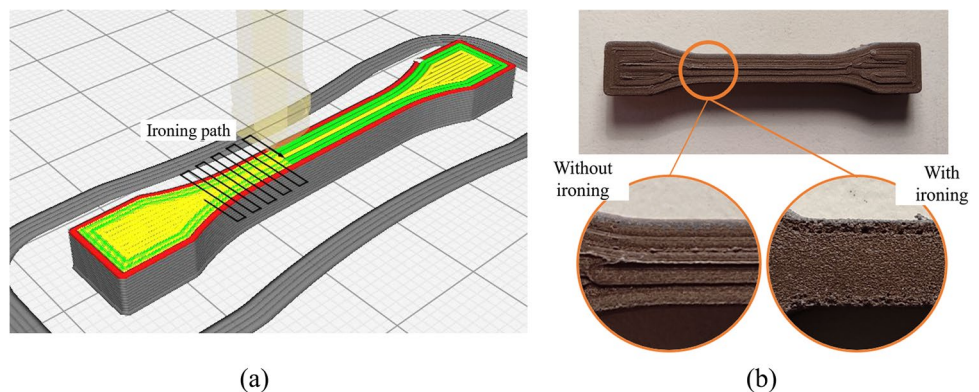
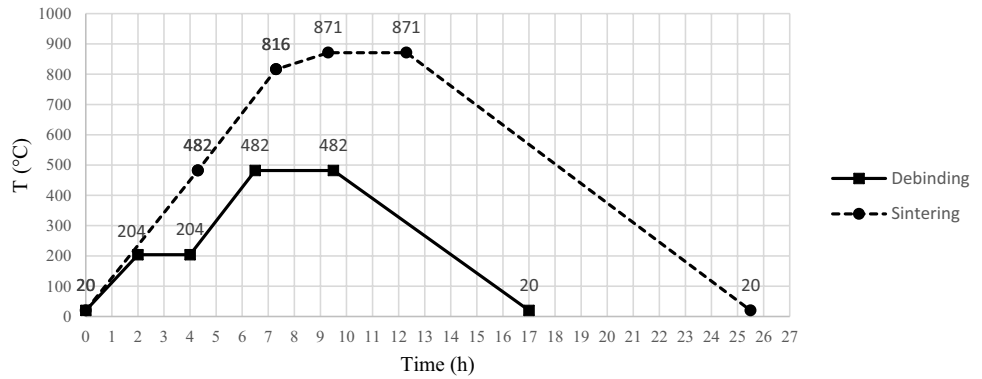


Fig. 5 Temperature profiles of the heat treatments adopted for the debinding and sintering processes, as suggested by The Virtual Foundry



use of powdered carbon allows for increased sintering temperatures.

2.4 Material characterization

The Shapiro-Wilk (SW) normality test, algorithm AS R94 [58], was used to verify whether the collected data followed a normal distribution. Where applicable, the one-way ANOVA method was used in combination with Tukey's Honestly Significant Difference test, to evaluate the significance of the data differences.

Full factorial regression was used to assess significant differences among sets and evaluate the influence of nozzle temperature, the pattern of intermediate layers, and ironing on the ultimate tensile strength.

The following subsections describe the procedures and methods used to characterize density, shrinkage, porosity, and tensile properties.

2.4.1 Evaluation of density, shrinkage, and porosity

The densities of the green and sintered parts were estimated on three prismatic specimens for each set by weighing the samples with an analytic PLC 200BC bench scale (G&G GmbH, Kaarst, Germany), which has a capacity of 200 g and an accuracy of 0.001 g. The density was calculated as the ratio of the weight to the volume of the specimens. Three distinct measurements for each specimen were collected with a twentieth caliper for each direction corresponding to different points for the green and brown geometries, and the average values were evaluated.

The porosities were instead evaluated on three sintered dog-bone specimens for each set. The specimens were cut with a diamond disk cutting blade, cold incorporated in a polymeric resin, and mechanically ground and sequentially polished using silicon carbide (SiC) grinding papers of decreasing grit size (120, 320, 500, 800, and 1200). Three different sections corresponding to the central part of the specimen were analyzed using the inverted optical microscope Leica DMI3000 M with a 10× objective.

Regions indicating porosities were identified using a thresholding algorithm using MATLAB software.

2.4.2 Evaluation of tensile properties

The mechanical characterization of the samples was carried out on five dog-bone specimens for each set by tensile tests using a Schenck universal testing machine with a 25 kN loading cell, a velocity of 0.5 mm/min, and a sampling frequency of 25 Hz. Two clamps were used to hold the samples, and a 10-mm extensometer was used to measure the elongation along the length of the specimen. Before the tensile tests, the cross-section was determined by averaging multiple measurements carried out using a twentieth caliper in the two directions. The data were analyzed using MATLAB software. In particular, the stress-strain curves for each parameter set were plotted, and the elastic modulus and tensile strength were determined.

3 Experimental results and discussion

3.1 Preliminary analysis

Among all the sets listed in Table 2, the printability issues have been preliminary assessed. Set H and I have been removed from the statistical analysis because corresponding green samples presented significant printability issues, e.g., over-extrusion and flashes (Fig. 6b, c). Set A, instead, was characterized by excessive inter-raster voids (Fig. 6a). However, this latter set has not been removed from the analysis since adopted as a reference set.

The SW normality test has been carried out on the ultimate tensile strength values of sets A:G to determine whether data is normally distributed. The test did not evidence non-normality (SW=0.9437, p -value > 0.05). ANOVA was used to identify possible significant differences with a confidence interval of 95%. The results highlighted a significant difference (F -value (6) = 7.55, p -value < 0.001) that has been further examined with a Tukey's pairwise comparison. Figure 7 reports the boxplot chart of



Fig. 6 Specimens presenting printability issues corresponding to set A (a), set H (b), and set I (c)

the ultimate tensile strength and a summary table reporting mean values and the Tukey’s grouping information. Mean values that do not share the same symbol are significantly different (95% confidence interval).

A full factorial regression has been computed for the sets from B to G with three factors (nozzle temperature, pattern of intermediate layers, and ironing), each with 2 levels. Set A has not been included in the regression since it introduces a parameter (flow rate) that has been kept constant due to printability issues.

Figure 8 reports, in a descending order, the Pareto chart of the absolute values related to the standardized effects of the parameters on the ultimate tensile strength. The bars greater than the red reference line highlight a significant effect on the ultimate tensile strength with a confidence level of 95%. The significant effects include the interaction pattern-ironing (BC) and the main effects of ironing (C) and pattern (B).

Figure 9 reports the main effects and the 2-way interaction effect of the main parameters on the ultimate tensile strength, obtained from the fitted linear model on the collected data ($R^2 = 85.29\%$, $R^2_{adj} = 78.86\%$). For the intermediate layers pattern, 0 means concentric and 1 means linear, while, for the ironing, 0 means that no ironing is used and 1 means that ironing is applied.

The results highlight that the ultimate tensile strength increases by using a linear pattern at the intermediate layers, and not activating the ironing.

In light of this preliminary analysis, further investigations about porosity, density, shrinkage, and mechanical behavior have been conducted on sets A–E. Sets F and G have not been further considered since not significantly different from sets B and D, but with a slightly lower mean ultimate tensile strength. The choice of limiting the number of sets to five was influenced by the necessity of optimizing the amount of material and handling time for the whole experimental effort.

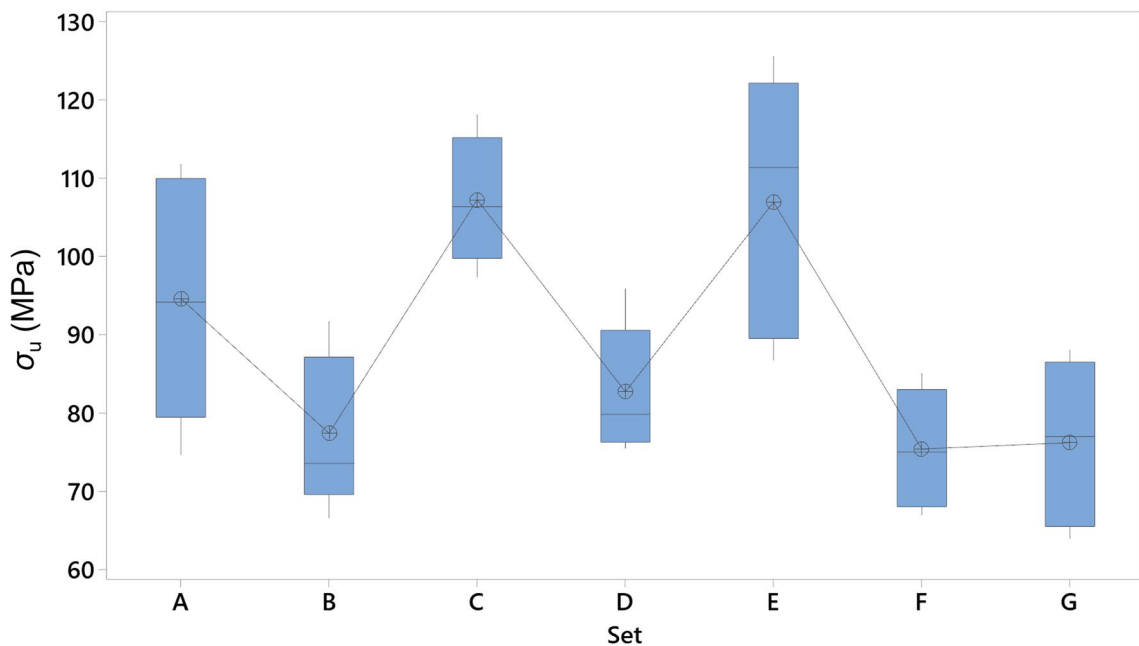


Fig. 7 Boxplot representation of the ultimate tensile strength for all the sets (from A to G) and grouping information table using the Tukey’s method and 95% confidence

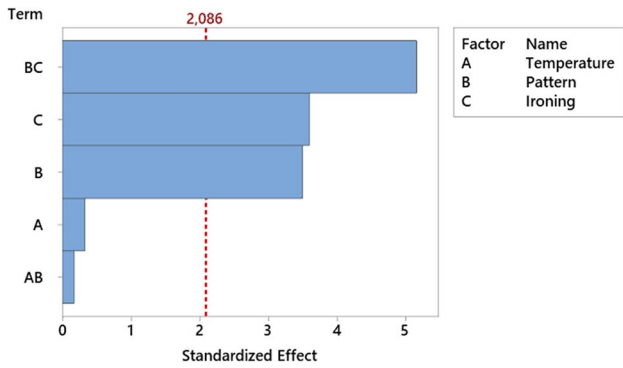


Fig. 8 Pareto chart of the effects on the ultimate tensile stress with a significance level $\alpha = 0.05$

3.2 Density, shrinkage, and porosity

Figure 10 reports an example of as-printed and sintered prismatic (Fig. 10a) and dog-bone (Fig. 10b) specimens. Figure 10b also shows a sintered specimen after the tensile test.

Figure 11 shows the section of the green part for the specimens of sets A and B (Fig. 11a), the same specimens incorporated in a polymeric resin (Fig. 11b) and processed with MATLAB to identify porosity (Fig. 11c). From the figures of the as-printed and sintered specimens, it is evident that set A

has the greatest porosity (dark areas in the specimen section) for the green part, but the least after sintering, if compared to set B. Although the pores produced during 3D printing reduce the density and overall quality of the specimen, they are beneficial in the gas evacuation because the green part provides pathways for the gases to escape more easily during the debinding process, reducing the likelihood of gas-related defects in the sintered parts (Fig. 11b).

Figure 12 lists the densities of the green and sintered samples for each parameter set studied. The results, which follow a normal distribution, are shown through the use of boxplots. The same figure also shows the shrinkage measurements on the x , y , and z axes.

With regard to the density of the green samples, set A showed a statistically significant difference (F -value(4) = 46.54, p -value < 0.001) compared to the other sets. The density values of sets B to E were consistently higher than those of set A, the reference set.

However, this higher density does not always result in a higher density of the respective sintered specimens. In this regard, the case of Set A is indicative. Although it had the lowest density after 3D printing (i.e., when it was a green sample), its density was the highest among all the considered sets after the sintering process. Also, it is worth noting that this set also underwent the most significant shrinkage, up

Fig. 9 Main effect (a) and interaction (b) plots of the significant parameters on the ultimate tensile strength. For the intermediate layers pattern, 0 means concentric and 1 means linear, while, for the ironing, 0 means that no ironing is used and 1 means that ironing is applied

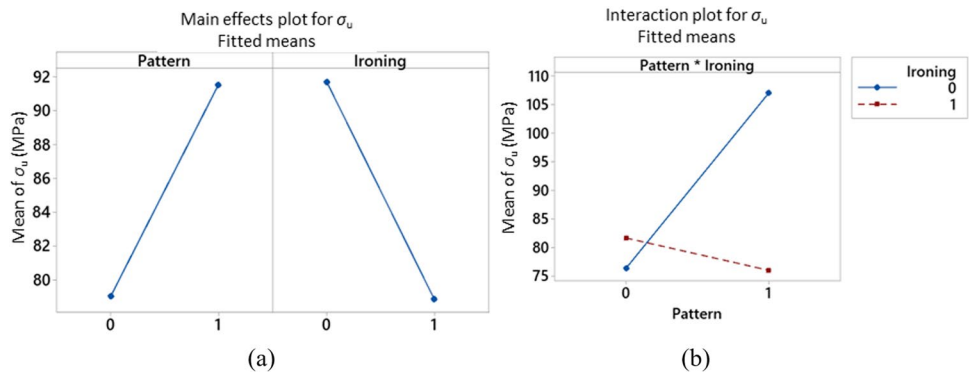
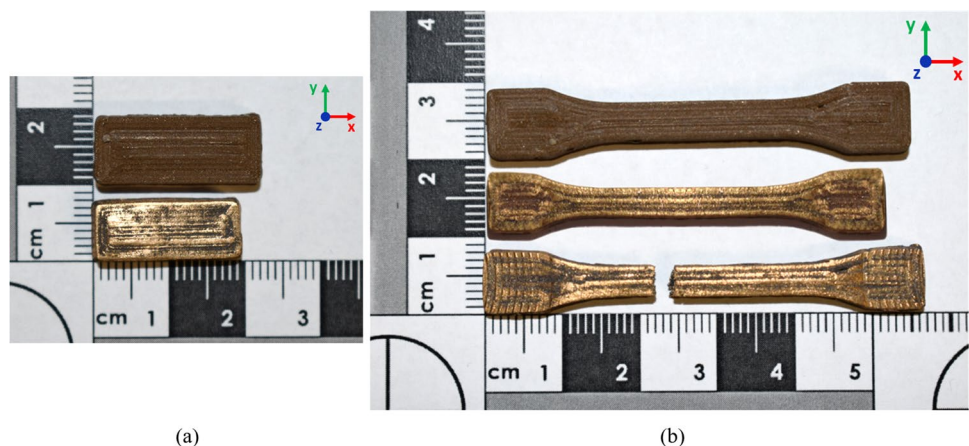


Fig. 10 Example of as-printed and sintered prismatic (a) and dog-bone (b) specimens; b also shows a sintered specimen after the tensile test



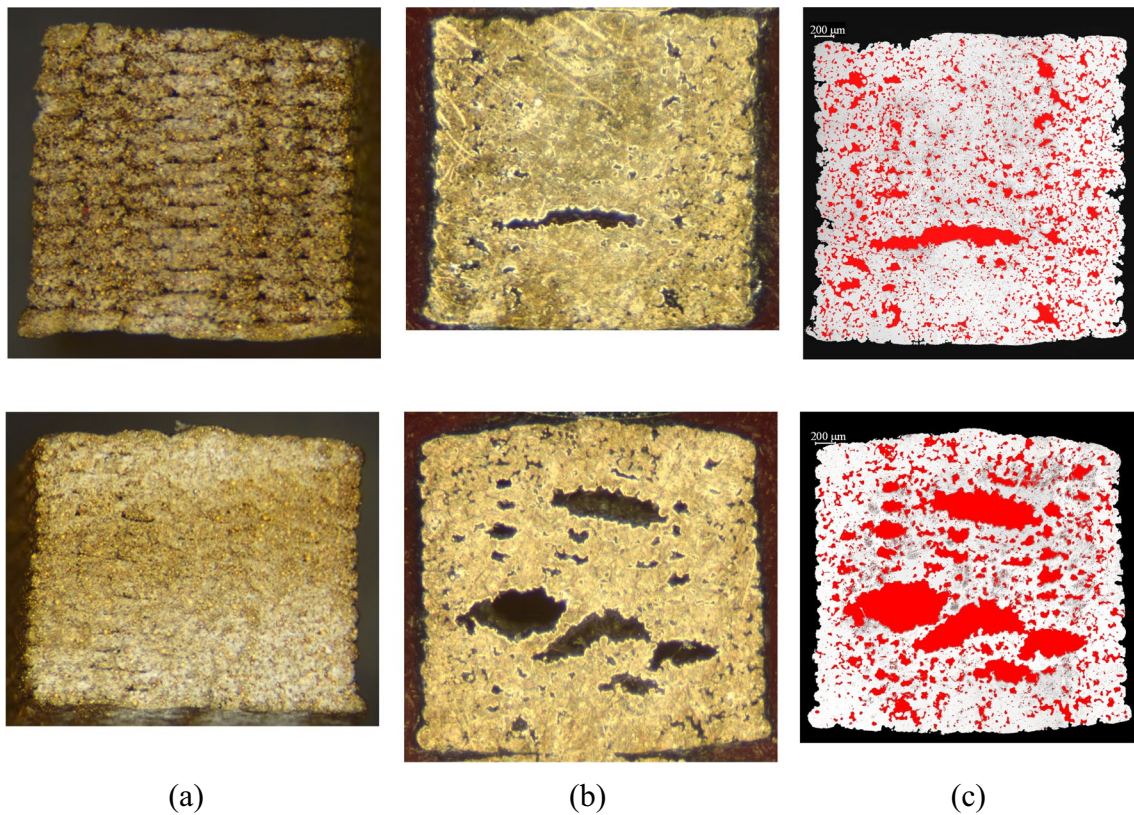
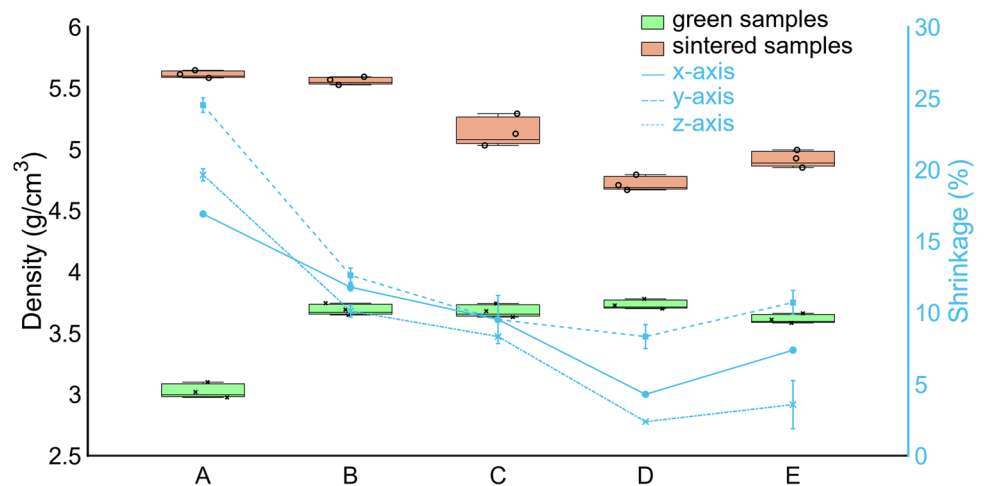


Fig. 11 Example of porosity for sets A and B before (a) and after sintering (b). The sintered specimen is incorporated in the polymeric resin and analyzed with MATLAB to identify porosities highlighted in red (c)

Fig. 12 Boxplot representation of the densities of green and sintered samples for all sets (from A to E). The shrinkage after sintering is also reported for each set along the *x*-, *y*- and *z*-axes



to approximately 25%. This confirms that when the PLA degrades, the lower density in set A in its green condition enables a better evacuation of the gases released during the debinding stage. However, the resulting high shrinkage values could undermine the process feasibility because the accuracy of the manufactured geometries may be unacceptable for most applications. Furthermore, with respect to

shrinkage, it can also be observed that for all sets, it is less pronounced on the *z*-axis and that, in general, as the density of the green samples increases, the shrinkage after sintering decreases. This is the case of set D, where the use of ironing increases the density of the green specimens. However, this higher density has a negative effect on the gas evacuation during the debinding phase, that remains trapped in the

specimen, resulting in lower density in the sintered sample. Shrinkage is closely related to the printing porosity of the green parts along the various directions. Along the *z* axis, for example, the size of the pores that are ideally created by the printing process can be associated with the layer thickness (0.3 mm in the present work). In-plane (*x* and *y* directions) porosities are instead mostly influenced by the line width (0.6 mm in this work) and by the infill pattern. This may explain why the material shrinks more along in-plane directions than along *z* during the thermal debinding and sintering processes. A lower shrinkage along *z* was also observed in [21], where the authors use the same bronze filament of the present research.

Finally, from Fig. 12, it can be noted that, in general, the results are not characterized by a large spread (for densities in particular) and that considering both the density of the sintered parts and their shrinkage, sets B and C could represent the best trade-off.

Statistical analysis revealed that there was a significant difference among all the sets for the average values of shrinkage along the *x*-axis ($F\text{-value}(4) = 473.94$, $p\text{-value} < 0.001$), *y*-axis ($F\text{-value}(4) = 36.90$, $p\text{-value} < 0.001$), and *z*-axis ($F\text{-value}(4) = 22.59$, $p\text{-value} < 0.01$). In particular, the shrinkage results of set A were consistently significantly higher than those of the other sets.

Figure 13 reports, in boxplot form, the porosity of sintered samples. Set A had the lowest porosity and its value is approximately 16%, meaning that 16% of the area of the analyzed sections is composed of voids. Conversely, the highest porosities were associated with set B and set E. The porosity values for these sets were about double that of set A. Sets C and D had intermediate porosities. However, the lowest porosity of set A must be considered by taking into account the considerable shrinkage described above for this set.

3.3 Mechanical characterization

Figure 14 reports the ultimate tensile strength (Fig. 14a) and the elastic modulus (Fig. 14b) of the sintered samples for each parameter set. For the selected five sets (A:E), the SW normality test was conducted to determine whether data were normally distributed. The test did not show evidence of non-normality ($SW=0.9575$, $p\text{-value} > 0.100$).

The ultimate tensile strengths for all parameter sets were significantly higher than the PLA tensile strength, which is about 50 MPa, while the tested metal specimens had, in the worst case, an average tensile strength of about 80 MPa. Sets C and E had higher average failure strengths than set A. Finally, sets C and E were characterized by average values

Fig. 13 Boxplot representation of the porosities of the sintered samples for all sets (from A to E)

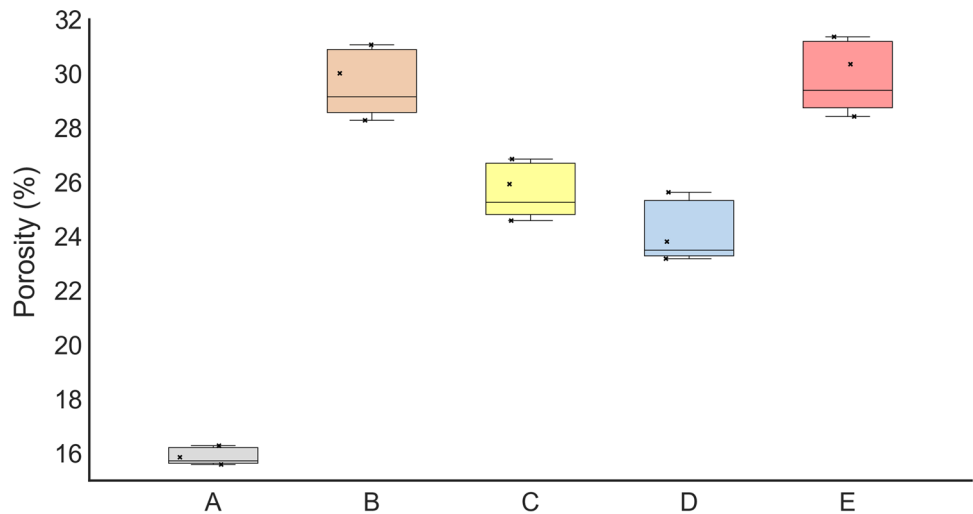
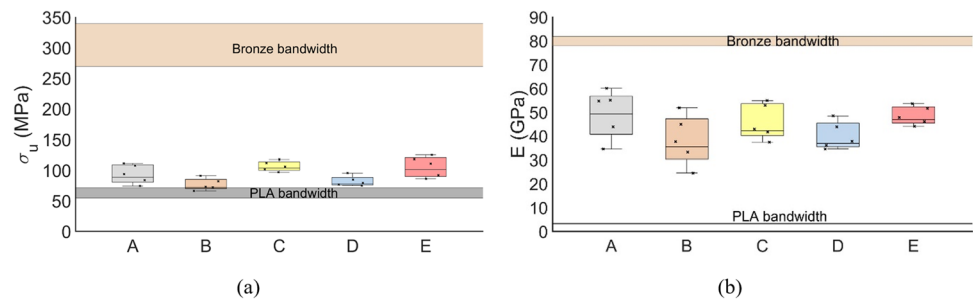


Fig. 14 Boxplot representation of tensile strength (a) and elastic modulus (b) for all sets (from A to E)



of tensile strength above 100 MPa. These two latter sets also showed a statistically significant pairwise difference compared to sets D and B (F -value(4)=6.14, p -value<0.01), which had the worst results in terms of ultimate tensile strength.

The results were even more remarkable with regard to the elastic modulus. In the case of the set with the lowest mean value (set B), the elastic modulus was at its lowest approximately 26 GPa. The highest and lowest mean values can be ascribed to sets A (49.7 GPa) and B (38.5 GPa). However, the spread between the different tests was high for both sets A (35–60 GPa) and B (26–52 GPa). All other sets showed a more limited spread of values, and sets C and E had mean values greater than 40 GPa. The differences in the elastic modulus among the datasets, however, were not statistically significant, as attested by the one-way ANOVA analysis. It is worth noting that for all the analyzed sets, the values of the elastic modulus were considerably higher than those of PLA (2–3 GPa) and polymers in general. Although these values do not reach those typical of the same type of CuSn12 bronze obtained by casting (78–82 GPa), they are comparable with those typical of other metals (e.g., magnesium and tin).

Table 4 reports the mechanical characterization results as mean and standard deviation values of elastic modulus, tensile strength, and elongation at break for all of the tested sets. Sets C and E behave similarly and produce the best results

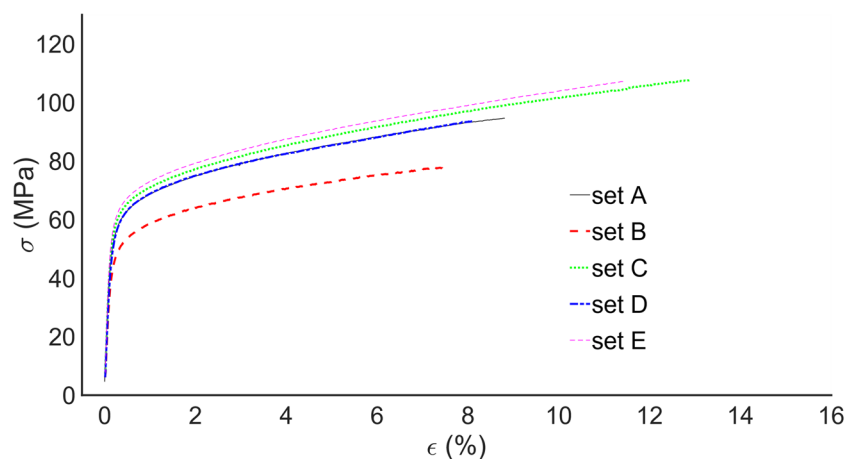
in terms of strength and strain. Set A has an intermediate level of strength and strain. On the other hand, sets B and D have the lowest values for elastic modulus, ultimate tensile strength, and elongation at break. The statistical analysis on elongation at break confirms that the most significant difference emerges between sets B and C (F -value(4)=3.32, p -value<0.05).

Figure 15 shows the average stress-strain curves for each set, providing an overview of all the specimen types tested and allowing a graphical comparison of mechanical and deformation behavior. Sets C and E have the highest ultimate tensile strength and strain at break. Sets A and D exhibit intermediate and nearly superimposable mechanical behaviors, while set B exhibits the worst. In all cases, the material showed good stiffness and ductile behavior. It is worth noting that most deformation has a plastic nature. This last characteristic must be highlighted because generally sintered materials are characterized by limited elongations and brittle behavior. This could be ascribed to a good coalescence between the bronze powder particles. For all the sets, the bronze specimens reached significant elongations at failure: from approximately 7% (set B) up to 13% (set C). The obtained results are remarkable, also considering that the same type of CuSn12 bronze, obtained by casting, has elongation values between 3 and 7% (Ansys Granta Edu-Pack 2021 R2, database: level 3). This factor is crucial for

Table 4 Mean and standard deviation values of elastic modulus, tensile strength, and elongation at break for all the sets

	Elastic modulus E (GPa)		Ultimate tensile strength σ_u (MPa)		Elongation at break ϵ_u (%)	
	Mean	St. deviation	Mean	St. deviation	Mean	St. deviation
Set A	49.73	10.32	94.59	15.68	8.82	2.22
Set B	38.53	10.51	77.40	9.81	7.29	1.83
Set C	46.02	7.58	107.23	8.17	13.11	2.27
Set D	40.23	5.84	82.69	8.24	8.12	4.64
Set E	48.70	3.92	106.92	16.78	11.47	3.14

Fig. 15 Average stress-strain curves for the sets studied



expanding the material's potential applications and ensuring higher levels of safety throughout use.

4 Conclusions

The MEAM technology is of increasing interest for metal additive manufacturing. It represents a valid alternative for low-cost metal production by retaining the advantages of other additive manufacturing technologies and guaranteeing a certain flexibility in the use of different types of metals. In the present study, the influence of three printing parameters (nozzle temperature, pattern of intermediate layers, and ironing) was tested and compared with a reference set obtained by adopting the printing parameters suggested by the filament manufacturer.

The results showed that as the density of the green samples increased, the shrinkage after sintering, as well as density, decreased. On the other hand, higher porosities on green parts resulted in higher shrinkage and density after sintering. Limited shrinkage is of utmost importance for the industrial scalability of a manufacturing process. It guarantees a more reliable process even for complex geometries, lower warping, and the possibility of having smaller and more controlled geometric and dimensional tolerances.

The parameters that most influenced the density increase of the green specimens were the flow rate, and ironing. In particular, an increase in flow rate and the addition of ironing determined an increase in density.

With respect to the mechanical properties, it can be observed that the extrusion line pattern of intermediate layers has a more positive effect on the ultimate tensile strength than the concentric pattern regardless of the temperature used. However, the results of the elastic modulus were not significantly influenced by the variation in the parameters studied. Finally, analysis of the stress-strain curves shows that the extrusion line pattern also has a positive influence on the elongations reached at the break, making the material more ductile. In general, all sets exhibit excellent mechanical performance and properties, and the bronze obtained has a notable ultimate tensile strength, high stiffness, and a greater elongation at break than that of cast bronze of the same CuSn12 type, with average strain values up to about 13% (i.e., approximately the double of the cast CuSn12). This aspect is very important to widen the possibilities of the application of the material, thereby guaranteeing greater safety conditions for its use. Furthermore, the present research activity aims to broaden the knowledge of low-cost 3D printing of highly filled metal filaments to manufacture parts with significant mechanical properties. This aspect will push forward the use of MEAM technology for industrial applications, increasingly

representing a feasible alternative to currently more consolidated but expensive technologies such as PBF or DED. Future research could be aimed at studying the influence of bronze post-processing treatment parameters. Furthermore, the approach proposed for the development of printing parameter sets and the multiscale characterization of the obtained material could be extended to a wider range of new and more advanced materials.

Acknowledgements We wish to thank Dr. Massimo Tazioli for his support in laboratory activities.

Author contribution All authors contributed to the study's conception and design, material preparation, data collection, and analysis. All authors read and approved the final manuscript.

Funding Open access funding provided by Università di Pisa within the CRUI-CARE Agreement. This work is supported by the Università di Pisa under the "PRA – Progetti di Ricerca di Ateneo" (Institutional Research Grants) - Project no. PRA_2022_23_ "Optimization of extrusion-based additive manufacturing for metallic and ceramic parts."

Declarations

Competing interests The authors declare no competing interests.

Open Access This article is licensed under a Creative Commons Attribution 4.0 International License, which permits use, sharing, adaptation, distribution and reproduction in any medium or format, as long as you give appropriate credit to the original author(s) and the source, provide a link to the Creative Commons licence, and indicate if changes were made. The images or other third party material in this article are included in the article's Creative Commons licence, unless indicated otherwise in a credit line to the material. If material is not included in the article's Creative Commons licence and your intended use is not permitted by statutory regulation or exceeds the permitted use, you will need to obtain permission directly from the copyright holder. To view a copy of this licence, visit <http://creativecommons.org/licenses/by/4.0/>.

References

1. Frazier WE (2014) Metal additive manufacturing: a review. *J Mater Eng Perform* 23(6):1917–1928. <https://doi.org/10.1007/s11665-014-0958-z>
2. Kok Y, Tan XP, Wang P, Nai MLS, Loh NH, Liu E et al (2018) Anisotropy and heterogeneity of microstructure and mechanical properties in metal additive manufacturing: a critical review. *Mater Des* 139:565–586. <https://doi.org/10.1016/j.matdes.2017.11.021>
3. Herzog D, Seyda V, Wycisk E, Emmelmann C (2016) Additive manufacturing of metals. *Acta Mater* 117:371–392. <https://doi.org/10.1016/j.actamat.2016.07.019>
4. Khorasani A, Gibson I, Veetil JK, Ghasemi AH (2020) A review of technological improvements in laser-based powder bed fusion of metal printers. *Int J Adv Manuf Technol* 108(1-2):191–209. <https://doi.org/10.1007/s00170-020-05361-3>
5. Sing SL, Yeong WY (2020) Laser powder bed fusion for metal additive manufacturing: perspectives on recent developments. *Virtual Phys Prototyp* 15(3):359–370. <https://doi.org/10.1080/17452759.2020.1779999>

6. Liu ZG, Wang YQ, Wu BC, Cui CZ, Guo Y, Yan C (2019) A critical review of fused deposition modeling 3D printing technology in manufacturing polylactic acid parts. *Int J Adv Manuf Technol* 102(9-12):2877–2889. <https://doi.org/10.1007/s00170-019-03332-x>
7. Samykano M, Selvamani SK, Kadirgama K, Ngui WK, Kanagaraj G, Sudhakar K (2019) Mechanical property of FDM printed ABS: influence of printing parameters. *Int J Adv Manuf Technol* 102(9-12):2779–2796. <https://doi.org/10.1007/s00170-019-03313-0>
8. Rane K, Strano M (2019) A comprehensive review of extrusion-based additive manufacturing processes for rapid production of metallic and ceramic parts. *Adv Manuf.* 7(2):155–173. <https://doi.org/10.1007/s40436-019-00253-6>
9. Nurhuda AI, Supriadi S, Whulanza Y, Saragih AS (2021) Additive manufacturing of metallic based on extrusion process: a review. *J Manuf Process* 66:228–237. <https://doi.org/10.1016/j.jmapro.2021.04.018>
10. Suwanpreecha C, Manonukul A (2022) A review on material extrusion additive manufacturing of metal and how it compares with metal injection moulding. *Metals-Basel.* 12(3). <https://doi.org/10.3390/Met12030429>
11. Wu GH, Langrana NA, Sadanji R, Danforth S (2002) Solid free-form fabrication of metal components using fused deposition of metals. *Mater Des* 23(1):97–105. [https://doi.org/10.1016/S0261-3069\(01\)00079-6](https://doi.org/10.1016/S0261-3069(01)00079-6)
12. Wu GH, Langrana NA, Rangarajan S, McCuiston R, Sadanji R, Danforth S et al (1999) Fabrication of metal components using FDMet: Fused deposition of metals. *Sol Freeform Fabric:775–782*
13. Hasib AG, Niazorau S, Xu WH, Niverty S, Kublik N, Williams J et al (2021) Rheology scaling of spherical metal powders dispersed in thermoplastics and its correlation to the extrudability of filaments for 3D printing. *Addit Manuf:41.* <https://doi.org/10.1016/J.Addma.2021.101967>
14. Singh P, Balla VK, Tofangchi A, Atre SV, Kate KH (2020) Printability studies of Ti-6Al-4V by metal fused filament fabrication (MF3). *Int J Refract Hard Met:91.* <https://doi.org/10.1016/J.Ijrmhm.2020.105249>
15. Cerejo F, Gatoes D, Vieira MT (2021) Optimization of metallic powder filaments for additive manufacturing extrusion (MEX). *Int J Adv Manuf Technol* 115(7-8):2449–2464. <https://doi.org/10.1007/s00170-021-07043-0>
16. Gonzalez-Gutierrez J, Cano S, Schuschnigg S, Kukla C, Sapkota J, Holzer C (2018) Additive manufacturing of metallic and ceramic components by the material extrusion of highly-filled polymers: a review and future perspectives. *Materials.* 11(5). <https://doi.org/10.3390/Ma11050840>
17. Craft DF, Lentz J, Armstrong M, Foster M, Gagneur J, Harrington D et al (2020) Three-dimensionally printed on-skin radiation shields using high-density filament. *Pract Radiat Oncol* 10(6):E543–EE50. <https://doi.org/10.1016/j.prro.2020.03.012>
18. Zhang ZC, Femi-Oyetero J, Fidan I, Ismail M, Allen M (2021) Prediction of dimensional changes of low-cost metal material extrusion fabricated parts using machine learning techniques. *Metals-Basel.* 11(5). <https://doi.org/10.3390/Met11050690>
19. Lu Z, Ayeni OI, Yang XH, Park HY, Jung YG, Zhang J (2020) Microstructure and phase analysis of 3D-printed components using bronze metal filament. *J Mater Eng Perform* 29(3):1650–1656. <https://doi.org/10.1007/s11665-020-04697-x>
20. Mohammadzadeh M, Lu H, Fidan I, Tantawi K, Gupta A, Hasanov S et al (2020) Mechanical and thermal analyses of metal-PLA components fabricated by metal material extrusion. *Inventions* 5(3). <https://doi.org/10.3390/inventions5030044>
21. Wei XY, Behm I, Winkler T, Scharf S, Li XJ, Bahr R (2022) Experimental study on metal parts under variable 3D printing and sintering orientations using bronze/PLA hybrid filament coupled with fused filament fabrication. *Materials.* 15(15). <https://doi.org/10.3390/Ma15155333>
22. Santos C, Gatoes D, Cerejo F, Vieira MT (2021) Influence of metallic powder characteristics on extruded feedstock performance for indirect additive manufacturing. *Materials.* 14(23). <https://doi.org/10.3390/Ma14237136>
23. Hwang S, Reyes EI, Moon K-s, Rumpf RC, Kim NS (2015) Thermo-mechanical characterization of metal/polymer composite filaments and printing parameter study for fused deposition modeling in the 3D printing process. *J Electron Mater* 44(3):771–777. <https://doi.org/10.1007/s11664-014-3425-6>
24. Terry S, Fidan I, Tantawi K (2021) Preliminary investigation into metal-material extrusion. *Prog Addit Manuf* 6(1):133–141. <https://doi.org/10.1007/s40964-020-00151-5>
25. Redondo E, Pumera M (2021) Fully metallic copper 3D-printed electrodes via sintering for electrocatalytic biosensing. *Appl Mater Today* 25:101253. <https://doi.org/10.1016/j.apmt.2021.101253>
26. Cheng CH, Loh CC, Zhang YJ (2022) Simulation of metallic parts by 3D printing using metallic powder-poly lactide composite filament. *Prog Addit Manuf* 7(3):495–508. <https://doi.org/10.1007/s40964-022-00287-6>
27. Guan XN, Xu XN, Kuniyoshi R, Zhou HH, Zhu YF (2018) Electromagnetic and mechanical properties of carbonyl iron powders-PLA composites fabricated by fused deposition modeling. *Mater Res Express* 5(11). <https://doi.org/10.1088/2053-1591/Aadce4>
28. Mousapour M, Salmi M, Klemettinen L, Partanen J (2021) Feasibility study of producing multi-metal parts by fused filament fabrication (FFF) technique. *J Manuf Process* 67:438–446. <https://doi.org/10.1016/j.jmapro.2021.05.021>
29. Thompson Y, Gonzalez-Gutierrez J, Kukla C, Felfer P (2019) Fused filament fabrication, debinding and sintering as a low cost additive manufacturing method of 316L stainless steel. *Addit Manuf.:30.* <https://doi.org/10.1016/J.Addma.2019.100861>
30. Wagner MA, Hadian A, Sebastian T, Clemens F, Schweizer T, Rodriguez-Arbaizar M et al (2021) Fused filament fabrication of stainless steel structures - from binder development to sintered properties. *Addit Manuf:102472.* <https://doi.org/10.1016/j.addma.2021.102472>
31. Kurose T, Abe Y, Santos MVA, Kanaya Y, Ishigami A, Tanaka S et al (2020) Influence of the layer directions on the properties of 316L stainless steel parts fabricated through fused deposition of metals. *Materials.* 13(11):10.3390/Ma13112493s
32. Sadaf M, Bragaglia M, Nanni F (2021) A simple route for additive manufacturing of 316L stainless steel via fused filament fabrication. *J Manuf Process* 67:141–150. <https://doi.org/10.1016/j.jmapro.2021.04.055>
33. Wang Y, Zhang L, Li X, Yan Z (2021) On hot isostatic pressing sintering of fused filament fabricated 316L stainless steel - Evaluation of microstructure, porosity, and tensile properties. *Mater Lett:296.* <https://doi.org/10.1016/J.Matlet.2021.129854>
34. Ait-Mansour I, Kretzschmar N, Chekurov S, Salmi M, Rech J (2020) Design-dependent shrinkage compensation modeling and mechanical property targeting of metal FFF. *Prog Addit Manuf* 5(1):51–57. <https://doi.org/10.1007/s40964-020-00124-8>
35. Rosnitschek T, Seefeldt A, Alber-Laukant B, Neumeyer T, Altstadt V, Tremmel S (2021) Correlations of geometry and infill degree of extrusion additively manufactured 316L stainless steel components. *Materials.* 14(18). <https://doi.org/10.3390/Ma14185173>
36. Moritzer E, Elsner CL, Schumacher C (2021) Investigation of metal-polymer composites manufactured by fused deposition modeling with regard to process parameters. *Polym Compos* 42(11):6065–6079. <https://doi.org/10.1002/pc.26285>
37. Quarto M, Carminati M, D'Urso G (2021) Density and shrinkage evaluation of AISI 316L parts printed via FDM process. *Mater*

- Manuf Process 36(13):1535–1543. <https://doi.org/10.1080/10426914.2021.1905830>
38. Caminero MA, Romero A, Chacon JM, Nunez PJ, Garcia-Plaza E, Rodriguez GP (2021) Additive manufacturing of 316L stainless-steel structures using fused filament fabrication technology: mechanical and geometric properties. *Rapid Prototyp J* 27(3):583–591. <https://doi.org/10.1108/Rpj-06-2020-0120>
 39. Caminero MA, Gutierrez AR, Chacon JM, Garcia-Plaza E, Nunez PJ (2022) Effects of fused filament fabrication parameters on the manufacturing of 316L stainless-steel components: geometric and mechanical properties. *Rapid Prototyp J* 28(10):2004–2026. <https://doi.org/10.1108/Rpj-01-2022-0023>
 40. Tosto C, Tirillo J, Sarasini F, Cicala G (2021) Hybrid metal/polymer filaments for fused filament fabrication (FFF) to print metal parts. *Appl Sci* 11(4). <https://doi.org/10.3390/App11041444>
 41. Jiang D, Ning F (2022) Anisotropic deformation of 316L stainless steel overhang structures built by material extrusion based additive manufacturing. *Addit Manuf.* 50:102545. <https://doi.org/10.1016/j.addma.2021.102545>
 42. Liu B, Wang YX, Lin ZW, Zhang T (2020) Creating metal parts by fused deposition modeling and sintering. *Mater Lett*:263. <https://doi.org/10.1016/J.Matlet.2019.127252>
 43. Gonzalez-Gutierrez J, Arbeiter F, Schlauf T, Kukla C, Holzer C (2019) Tensile properties of sintered 17-4PH stainless steel fabricated by material extrusion additive manufacturing. *Mater Lett* 248:165–168. <https://doi.org/10.1016/j.matlet.2019.04.024>
 44. Godec D, Cano S, Holzer C, Gonzalez-Gutierrez J (2020) Optimization of the 3D printing parameters for tensile properties of specimens produced by fused filament fabrication of 17-4PH stainless steel. *Materials*. 13(3). <https://doi.org/10.3390/Ma13030774>
 45. Abe Y, Kurose T, Santos MVA, Kanaya Y, Ishigami A, Tanaka S et al (2021) Effect of layer directions on internal structures and tensile properties of 17-4PH stainless steel parts fabricated by fused deposition of metals. *Materials*. 14(2). <https://doi.org/10.3390/Ma14020243>
 46. Zhang YZ, Bai SY, Riede M, Garratt E, Roch A (2020) A comprehensive study on fused filament fabrication of Ti-6Al-4V structures. *Addit Manuf*:34. <https://doi.org/10.1016/J.Addma.2020.101256>
 47. Singh P, Balla VK, Gokce A, Atre SV, Kate KH (2021) Additive manufacturing of Ti-6Al-4V alloy by metal fused filament fabrication (MF3): producing parts comparable to that of metal injection molding. *Prog Addit Manuf* 6(4):593–606. <https://doi.org/10.1007/s40964-021-00167-5>
 48. Singh P, Balla VK, Atre SV, German RM, Kate KH (2021) Factors affecting properties of Ti-6Al-4V alloy additive manufactured by metal fused filament fabrication. *Powder Technol* 386:9–19. <https://doi.org/10.1016/j.powtec.2021.03.026>
 49. BASF 3D printing solutions GmbH BASF metal filaments. <https://forward-am.com/material-portfolio/ultrafuse-filaments-for-fused-filaments-fabrication-fff/metal-filaments> (2022). Accessed 14 February 2022
 50. The virtual foundry. <https://www.thevirtualfoundry.com> (2021). Accessed 14 December 2021
 51. Hassan W, Farid MA, Tosi A, Rane K, Strano M. The effect of printing parameters on sintered properties of extrusion-based additively manufactured stainless steel 316L parts. *Int J Adv Manuf Technol* 2021;114(9-10):3057-3067. <https://doi.org/10.1007/s00170-021-07047-w>
 52. Babu GR, Junghans E, Andersen I, Lim YK, Lindstrom P (2021) Additive manufactured marine component - Ni Al bronze propeller. *Procedia Struct Integr* 34:20–25. <https://doi.org/10.1016/j.prostr.2021.12.039>
 53. Tavares SSM, Mota NM, da Igreja HR, Barbosa C, Pardal JM (2021) Microstructure, mechanical properties, and brittle fracture of a cast nickel-aluminum-bronze (NAB) UNS C95800. *Eng Fail Anal*:128. <https://doi.org/10.1016/j.engfailanal.2021.105606>
 54. Popescu D, Zapciu A, Amza C, Baciu F, Marinescu R (2018) FDM process parameters influence over the mechanical properties of polymer specimens: a review. *Polym Test* 69:157–166. <https://doi.org/10.1016/j.polymertesting.2018.05.020>
 55. Kerekes TW, Lim H, Joe WY, Yun GJ (2019) Characterization of process-deformation/damage property relationship of fused deposition modeling (FDM) 3D-printed specimens. *Addit Manufs.* 25:532–544. <https://doi.org/10.1016/j.addma.2018.11.008>
 56. Sardinha M, Vicente CMS, Frutuoso N, Leite M, Ribeiro R, Reis L (2021) Effect of the ironing process on ABS parts produced by FDM. *Mater Des Process Commun* 3(2):e151. <https://doi.org/10.1002/mdp2.151>
 57. Sapphire3D. <https://www.sapphire3d.com/> (2022). Accessed 22 March 2022.
 58. Royston P, Remark AS (1995) R94: a remark on algorithm AS 181: the W-test for normality. *J R Stat Soc: Ser C: Appl Stat* 44(4):547–551. <https://doi.org/10.2307/2986146>

Publisher's note Springer Nature remains neutral with regard to jurisdictional claims in published maps and institutional affiliations.